Journal of Molecular Catalysis A: Chemical 412 (2016) 67–77

Contents lists available at ScienceDirect

Journal of Molecular Catalysis A: Chemical

journal homepage: www.elsevier.com/locate/molcata

Photo-catalytic selectivity of anthranilic acid over iron oxide incorporated titania nanoparticles: Influence of the Fe^{2+}/Fe^{3+} ratio of iron oxide

Ya-Hui Chang, Chun-Chang Ou, Hui-Wen Yeh, Chung-Sung Yang*

Department of Applied Chemistry, National Chia Yi University, Chiayi 60004, Taiwan, ROC

ARTICLE INFO

Article history:
Received 22 August 2015
Received in revised form
28 November 2015
Accepted 1 December 2015
Available online 3 December 2015

Keywords:
Photocatalysis
TiO_2
Fe_2O_3
Selectivity

ABSTRACT

Iron oxide incorporated titania nanoparticles (FIT) with various atomic ratios of Fe/Ti, i.e. 3.53% (FIT-1), 8.3% (FIT-2), and 20.79% (FIT-3), are prepared to monitor the selectivity of photo-degradation for anthranilic acid (AA) in molecular level. In the FIT-1 route, the products obtained from the photo-degradation of AA are aniline, 4-aminophenol, and benzene. Since the surface of iron oxide domain in FIT-1 is fully reduced to FeO. The FeO, by trapping the photo-generated (e^-), acts as a Lewis base to facilitate the de-carboxylation reaction for AA to create aniline. It is noteworthy that the highly alkaline surface of FIT-1 executes the hydroxylation addition for AA to produce 4-aminophenol. In FIT-2, and FIT-3 routes, the surface of incorporated iron oxide is only partially reduced to FeO. After the photo-degradation of AA, the collected products are 2-aminobenzaldehyde, and benzene. In this route, the low spin (LS) Fe^{3+} ion in the Fe_2O_3 region adopts the photo-generated (e^-). The LS Fe^{3+} is reduced to stable LS Fe^{2+}, i.e. FeO. At this stage, the Fe_2O_3 domain acts as a Lewis acid to push forward the carbonyl reduction of AA to obtain 2-aminobenzaldehyde. In addition, the de-amination is contributed by the nucleorphilic attack of water molecule to the carbon atom of aromatic ring bonded to NH_2 group. After the de-amination reaction, the intermediate product is phenol. The following de-hydroxyl reaction by FeO domain proceeds immediately. The final product is benzene that is observed in all FIT involved catalytic routes.

1. Introduction

Solar application of photochemical oxidation methods is a convenient method for the treatment of highly contaminated effluents [1,2]. Among the available photochemical oxidation methods, the photo Fenton reaction (Fe^{2+}/H_2O_2/UV–vis) is the most economical way to treat the environmental or industry waste water [1–3]. Generally, the efficiency of the reaction depends mainly on the concentration of H_2O_2, molar ratio of [Fe^{2+}/H_2O_2], pH value, and reaction time [2,3]. The initial concentration of the pollutant and its character as well as the temperature, also have a substantial influence on the final efficiency [3]. The another censure is the yield of too many hydroxyl radicals besides the reaction, $Fe^{2+} + H_2O_2 \rightarrow Fe^{3+} + HO^- + {}^\bullet OH$ [4–6]. It is a paradox that the reaction is successfully used in environmental protection, but causes the damages to biomolecules and a variety of diseases, such as the DNA damage mediated by the active forms of hydroxyl radicals [7,8].

In the previous literature, most effort focuses on the synthesis of Fe/TiO_2 nanoparticles, i.e. $Fe_{1-x}Ti_xO_2$ nanoparticles. The preparation of iron oxide incorporated TiO_2 nanoparticles is few [9–11]. In this study, a novel nano-composite photocatalyst, iron oxide incorporated titania (FIT) nanoparticles is developed via a non-aqueous route with a tunable atomic ratio of Fe/Ti from 3.53% to 20.79% via a non-aqueous route as a solution for the dilemma. The tunable incorporating level of iron oxide not only flexibly adjusts the surface Lewis acidity of FIT, but also effectively avoids the agglomeration of composite nanoparticles. As mentioned in the previous paragraph, kinetic peculiarity of hydrogen peroxide in the reaction system is that iron catalyzes the univalent reduction of hydrogen peroxide to generate the neutral hydrogen oxide radicals and hydrogen oxide ions [5,6]. By use of the photo-generated ($e^- – h^+$) pair in TiO_2 region, the newly prepared FIT photocatalyst can perform the redox reaction: $O_2 + e^- \rightarrow O_2{}^{\bullet -}$, and $2\ O_2{}^{\bullet -} + 2\ H^+ \rightarrow OH^- + {}^\bullet OH + O_2$ to obtain the required hydrogen oxide radicals and hydrogen oxide ions for the reaction [12–15]. In this photocatalytic reaction, the hydrogen peroxide is excluded. Moreover, the photocatalytic selectivity of FIT

* Corresponding author. Fax: +886 5 271 7901.
E-mail address: csyang@mail.ncyu.edu.tw (C.-S. Yang).

http://dx.doi.org/10.1016/j.molcata.2015.12.001
1381-1169/

is tunable via adjusting the ratio of Fe^{2+}/Fe^{3+} in the incorporated iron oxide. By elimination of hydrogen peroxide in the photocatalytic reaction and control of the selectivity in photocatalytic route, the novel prepared FIT is a practical solution for the treatment of environmental organic pollutants.

2. Experimental

(a) Chemicals

Iron(III) acetylacetonate ($Fe(C_5H_7O_2)_3$, IAA) was obtained from Sigma–Aldrich, Titanium(IV) butoxide (TBO) were purchased from Fluka. Tetra-*n*-propylammonium bromide (TPAB) was got from Alfa Aesar. Reagent-grade ethylene glycol (EG, 99% Showa) was used without any further purification. HPLC grade methanol and reagent grade ethanol were obtained from Sigma–Aldrich, and were used as supplied.

(b) Synthesis and characterization of FIT

The FIT photocatalyst was synthesized by the reaction of IAA, TBO, and template TPAB in EG. A typical synthesis route for mole ratio of IAA:TBO = 0.1:1 is described as follows. TPAB 2.0 g, a limiting reagent, was mixed with 30 mL EG in a tri-neck bottle. The mixture was stirred for 20 min to dissolve the template TPAB completely in EG. The starting reagents IAA (0.207 g) was added into the EG/TPAB solvent. The temperature of solution was raised slowly from room temperature to refluxing temperature (180–190 °C) with a standard stirring speed of 250 rpm. After 20 min, the color of solution turned to clear. TBO (2.0 mL) was added into the clear solution. The color of the mixture was slowly changed from clear to orange–brown after 20 min refluxing. The orange–brown color remained for more than 48 h. The first aliquot withdrawal (3 mL) was taken at the 4th h. Each withdraw was washed twice with 10 mL of ethanol, and then transferred in 10 mL DI water to remove template residue. The final orange–brown precipitate was dried as a powder for further investigation.

3. Results

3.1. Characterization of FIT nanoparticles

The different amount of atomic ration of Fe/Ti from FIT-1 (Fe/Ti < 5%), FIT-2, (5% < Fe/Ti < 15%), to (FIT-3, 15% < Fe/Ti < 30%) were prepared for the study. The rate of growth of FIT nanocrystallites is highly dependent on the competition between titania and iron oxide crystalline seeds [12–15]. The partial positive charge on titanium (+0.63) in TBO is higher than that of iron (+0.46) in IAA [11,12]. Therefore, the nucleophilic attack between EG and TBO is earlier than that of EG and IAA. In addition, because the TBO has the advantage in concentration, the growing speed of titania crystallites is much larger than that of iron clusters.

(I) TEM and EDX of TEM

The TEM and high-resolution TEM (HR-TEM) images of FIT samples were used to study the crystallinity and detailed composition of these nanoparticles. A typical TEM image of FIT-1 collected at the 24th h, denoted as FIT-1–24 h, is given in Fig. 1(a). The product is calcinated at 400 °C for 1 h to remove EG. The size of iron oxide observed in this micrograph is smaller than 0.6 nm, marked by short arrows at upper left corner of Fig. 1(a). The titania part is well grown to be crystalline and the diameter is larger than 5 nm. The d-spacing of lattice fringes (0.305 nm), marked by A, matches the (1 0 1) crystal phases of anatase TiO_2. In the TEM image for FIT-2–24 h, Fig. 1(b), the heterogeneous iron oxide domains are clearly incorporated on the surface of TiO_2 nanoparticle. The selected area electron diffraction (SAED) of FIT-2–24 h is a ring pattern, meaning that FIT-2–24 h has a short-range crystalline structure (on the nano-scale) [11,12]. In the energy dispersive X-ray spectrum (EDX) of TEM for Fig. 1(a), two Ti peaks, (4.51 keV (Kα), 4.93 keV (Kβ)), and three Fe peaks (0.7 keV (Lα), 6.39 keV (Kα), 7.06 keV (Kβ)) are identified in FIT-1–24 h [14,15]. The gross atomic ratio of Fe/Ti is < 5% in FIT-1–24 h. The same characterization procedure is employed for FIT-2 (Fe/Ti < 10%) and FIT-3 (Fe/Ti < 25%).

(II) Powder XRD and Raman spectra

The gradual changes in the composition and the variations in crystallinity of FIT are monitored by powder X-ray diffraction (P-XRD). The FIT samples used for P-XRD are collected at the 24th h. These samples are denoted as FIT-1, FIT-2, and FIT-3 for clarity purpose.

The P-XRD of FIT-1 is given in Fig. 2(a). In the region of 10–80° (two theta), nine peaks match the (1 0 1), (0 0 4), (2 0 0), (1 0 5), (2 1 1), (2 0 4), (1 1 6), (2 2 0), and (2 1 5) of anatase TiO_2 [16a]. In addition, one peak matches (1 2 1) of brookite TiO_2 [16b]. The diffraction pattern shows that the main domain of FIT-1–24 h remains anatase TiO_2 structure. On the other hand, the iron oxide (Fe_3O_4) matrix is not evident in the P-XRD of FIT-1. A similar result of P-XRD pattern is observed in the P-XRD of FIT-2, and FIT-3.

The Raman spectrum is employed to investigate the incorporation behavior of iron oxide in TiO_2. Two samples, FIT-1 and FIT-3, are selected for Raman study. In FIT-1, six peaks, 144 cm^{-1}(E_g), 197 cm^{-1}(E_g), 399 cm^{-1} (B_{1g}), 515 cm^{-1}(A_{1g}), 519 cm^{-1}(B_{1g}), and 639 cm^{-1}(E_g), match the TiO_2 anatase structure, Fig. 2(b) [17]. The amount of iron oxide in FIT-1 is too little to be detected in Raman spectrum. In FIT-3, one new peak, 281 cm^{-1} is observed, which is assigned to E_{1g} of α-Fe_2O_3, Fig. 2(c) [18]. The six TiO_2 anatase peaks do not show any obvious shift in locations. The TiO_2 anatase domain obviously remains in FIT. The results agree with the data of P-XRD.

(III) X-ray photo-emission spectra (XPS)

The quantitative atomic ratios of Fe/Ti for FIT-1, FIT-2, and FIT-3 composite photocatalysts are measured by X-ray photoemission spectra (XPS). The region-wise XPS scan of FIT-1 is provided in Fig. 3, from 750 eV to 440 eV. Following a correction for sample charging, the binding energy (BE) values for TiO_2 are Ti 2s = 566.0 eV, Ti $2p_{1/2}$ = 465 eV, Ti $2p_{3/2}$ = 458.8 eV, Ti 3s = 63.1 eV, Ti 3p = 37.8 eV, and O 1s = 529.9 eV, O 2s = 23.0 eV. The BE values for iron oxide are Fe $2p_{1/2}$ = 724 eV, and Fe $2p_{3/2}$ = 708.8 eV. These data are in agreement with the values reported in the literature [19]. The elemental microanalysis data show that the atomic ratio (Fe/Ti) of Fe (1.13%)/Ti (31.97%) in FIT-1 is 3.53%. In FIT-2 samples, the Fe/Ti ratio of Fe (2.57%)/Ti (31.18%) is 8.24%. In the FIT-3 samples, the atomic ratio of Fe (6.18%)/Ti (29.76%) is 20.79%.

The commercial software, XPSPEAK 4.0, was acquired for the peak deconvolution. The selected peak was Fe $2p_{3/2}$ of XPS measured for FIT. The Shirley baseline subtraction method was applied before the peak deconvolution. The blow-up section for Fe $2p_{3/2}$, from 705 eV to 718 eV, has a broad band of interest. Theoretically, each component peak corresponds to a typical binding energy. After the deconvolution work, an iron $2p_{3/2}$ peak was judged to have two component peaks, P1 (Fe^{3+}), P2 (Fe^{2+}) and two satellite peaks, S1 and S2, to reach the minimum X^2 value, given in Fig. 4 [13–15,21,22]. The binding energy assigned for peak P1 (Fe^{3+}) is around 710.33–710.70 eV. For peak P2 (Fe^{2+}), the binding energy is in the range of 708.47–708.80 eV. The atomic ratio of Fe^{2+}/Fe^{3+} can be calculated precisely. The detail deconvoluted data and theX^2 values are provided in Table 1.

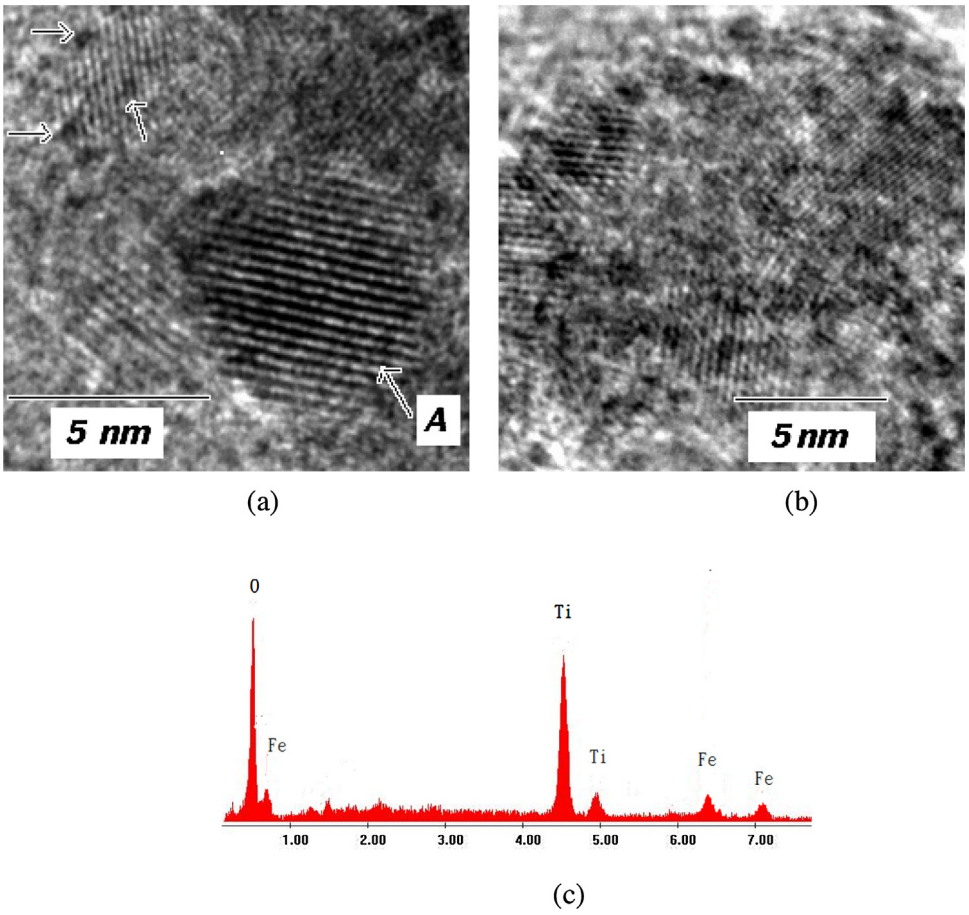

Fig 1. (a) A typical TEM image of FIT-1–24 h. The size of iron oxide is smaller than 0.5 nm, marked by short arrows. The d-spacing of lattice fringes (0.305 nm), marked by A, matches the (1 0 1) of anatase TiO_2. (b) A TEM image of FIT-2–24 h. The size of iron oxide is ~0.6–0.8 nm. (c) EDX spectra of Fig. 1(a). Two Ti peaks, (4.51 keV (Kα), 4.93 keV (Kβ)), and three Fe peaks (0.71 keV (Lα), 6.39 keV (Kα), 7.06 keV (Kβ)) are identified.

Table 1
The deconvoluted peak area, peak position (eV) and ΣX^2 value.

	FIT-1 (IAA:TBO = 0.05:1)	FIT-2 (IAA:TBO = 0.1:1)	FIT-3 (IAA:TBO = 0.25:1)
P1 (Fe^{3+})	2089.4 (710.70 eV)	2747.4 (710.33 eV)	3962.9 (710.52 eV)
P2 (Fe^{2+})	4152.9 (708.80 eV)	4556.6 (708.47 eV)	4630.9 (708.50 eV)
S1	318.24 (714.60 eV)	224.62 (714.87 eV)	216.24 (715.20 eV)
S2	823.28 (713.20 eV)	763.80 (712.70 eV)	997.3 (713.50 eV)
ΣX^2	0.125	0.0346	0.109

Background: Shirly method; smoothing: FFT 20%.
($X^2 = \Sigma[d^{exp} - d^{fit}]^2/\sigma^2$), d^{exp} = exp. data; d^{fit} = fitted data; σ^2 = square exp. uncertainties.

Basically, the Fe^{3+} ions and Fe^{2+} ions co-exist in all samples. One typical tendency of peak areas observed in the curve-fitting data is that the atomic ratio of Fe^{2+}/Fe^{3+} is inversely proportional to the amount of iron oxide in FIT. The ratio of peak area for Fe^{2+}:Fe^{3+} decreases from 1.99 (FIT-1), to 1.35 (FIT-2), and finally to1.17 (FIT-3). The oxidation state of divalent ion (Fe^{2+}) is the dominate valence state between Fe/Ti = 3.53% and Fe/Ti = 20.79%.

3.2. Photocatalytic degradation of anthranilic acid

The photoluminescence (PL) emission spectra were used to explore the adsorption ability and the photocatalytic mechanism of the organic anthranilic acid (AA) over FIT. The FIT samples were calcinated at 400 °C for 1 h before used in the photo-degradation reaction. The organic acid AA is an amphoteric species with complicate metabolism intermediates in organism beings. If released to air, AA will exist solely as a vapor in the atmosphere until photo-degraded by photochemically-produced hydroxyl radicals in air.

(I) Diffuse reflectance spectrum (DRS) of FIT

The selection of a suitable irradiation wavelength is essential to prove that the degradation of target compound is authentic by the photocatalyst. The 365 nm irradiation wavelength satisfies the cut-off band gap of diffuse reflectance spectrum (DRS) for FIT-3 (480 nm), FIT-2 (445 nm), and FIT-1 (410 nm), shown in Fig. 5. Since the band gap of α-Fe_2O_3 is 2.1 eV, the increase of the incorporated amount of iron oxide may lead to the red-shift of band gap observed in FIT samples. A similar result is also observed in previous research [17,18].

(II) Photo-degradation of adsorbed AA on FIT

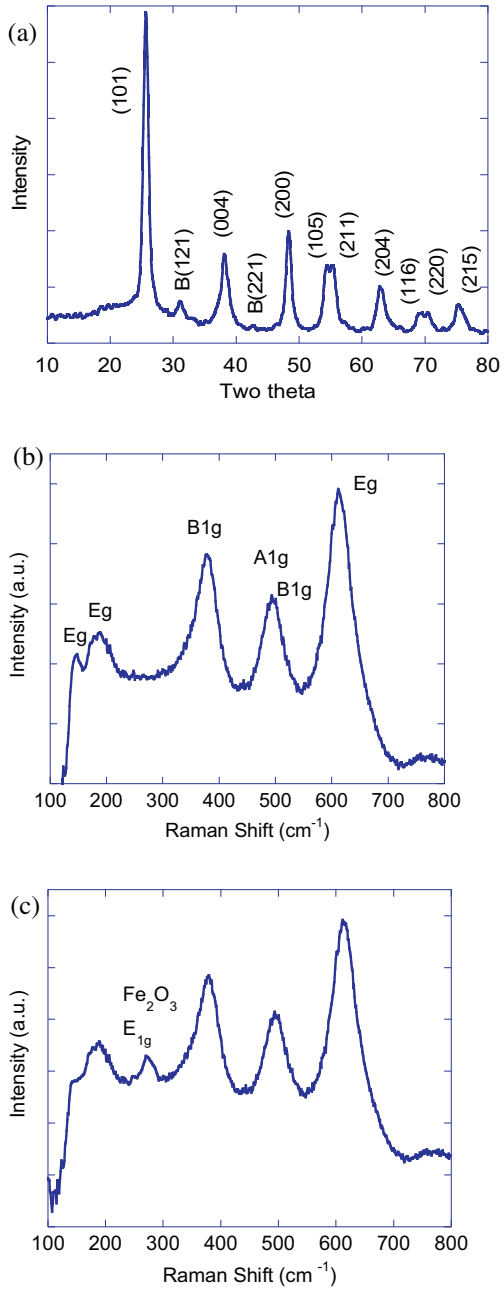

Fig. 2. (a) The P-XRD of FIT-1. Nine peaks match the (101), (004), (200), (105), (211), (204), (116), (220), and (215) of anatase TiO_2. Raman spectra for (b) FIT-1 and (c) FIT-3. In (b), six peaks, 144 cm^{-1}(E_g), 197 cm^{-1}(E_g), 399 cm^{-1}(B_{1g}), 515 cm^{-1}(A_{1g}), 519 cm^{-1}(B_{1g}), and 639 cm^{-1}(E_g), match the TiO_2 anatase structure. In (c), one new peak, 281 cm^{-1} is recorded, assigned to E_{1g} of α-Fe_2O_3.

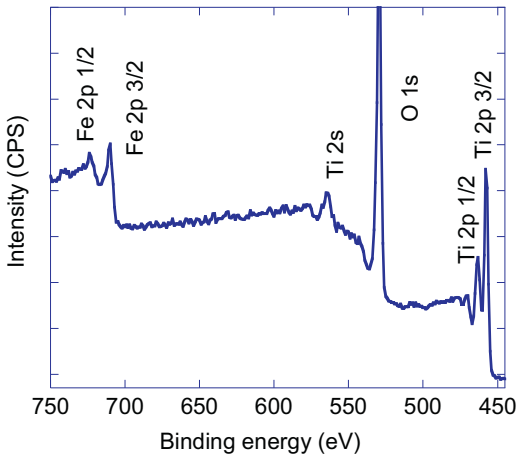

Fig. 3. The XPS spectrum of FIT-1, ranging from 750 eV to 440 eV.

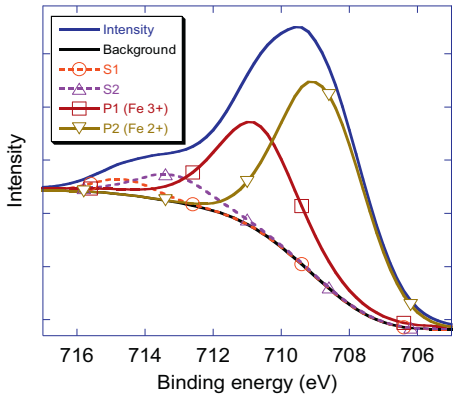

Fig. 4. The blow-up section of XPS for FIT-1, from 705 eV to 718 eV assigned to Fe $2p_{3/2}$. An iron $2p_{3/2}$ peak was judged to have two component peaks, P1 (Fe^{3+}), P2 (Fe^{2+}) and two satellite peaks, S1 and S2, to reach the minimum X^2 value.

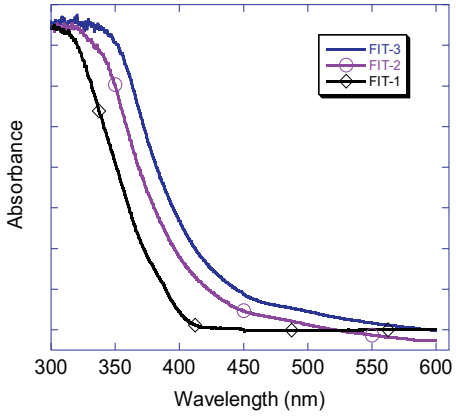

Fig. 5. The cut-off band gap of diffuse reflectance spectrum (DRS) for FIT-3 (480 nm), FIT-2 (445 nm), and FIT-1 (410 nm).

The self-degradation rate of AA is measured by the photoluminescence (PL) emission spectrum. During the 50 min irradiation, the intensity of PL decreases 1.23% (10th min), 2.18% (30th min), and 3.03% (50th min), respectively. The self-degradation rate constant (k_{self}), calculated from the plot of time-involved photo-reaction, is $(-)\ 6 \times 10^{-4}\ min^{-1}$. By deduction of the k_{self}, the rate constants (k_{cat}) derived from the plot will be the real rate constant.

The photocatalytic degradation routes of absorbed AA were explored by two routes for experimental purpose. One route is with high [AA]/[cat.] ratio, (AA:cat. = 1:0.67, denoted as route 1). The other route is with low [AA]/[cat.] ratio, (AA:cat. = 1:100, denoted as route 2). Each photocatalyst (route 1 = 10 mg, route 2 = 30 mg) was immersed in 30 mL AA stock solution (route 1 = 5×10^{-4} M, route 2 = 1×10^{-5} M). The immersed photocatalysts were bubbled with nitrogen before the UV irradiation (18 W, λ = 365 nm). The samples irradiated for 10 min were marked as series "a", i.e. FIT-1-a, FIT-2-a, and FIT-3-a. The other samples, irradiated for 20, 30, 40, and 50 min, were marked as series "b", "c", "d", and "e", respectively. The collected solutions were filtrated and the filtrates were analyzed by PL emission spectra to determine the concentration of non-degraded AA remained in the filtrate. A typical PL spectrum for photo-degradation of AA over FIT is provided in Fig. 6(a)

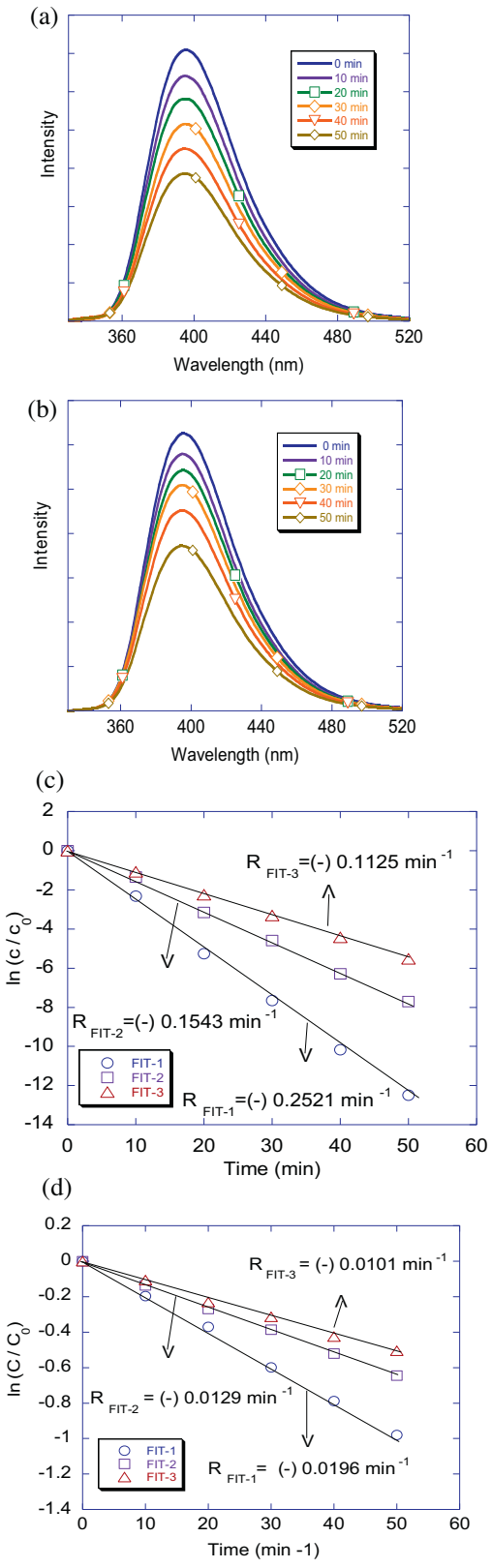

Fig. 6. PL spectra for photo-degradation of AA over FIT-1, (a) for route 1 (b) for route 2. One major peak between 340 and 520 nm, λ_{max} = 395 nm, was observed from 0 to 50 min under UV irradiation. (c) In route 1, the k_{cat} values of FIT-1 (0.252 min^{-1}), FIT-2 (0.154 min^{-1}), FIT-3 (0.113 min^{-1}) are in the ratio 1.00:0.61:0.45. (d) In route 2, the k_{cat} values of FIT-1 (0.00914 min^{-1}), FIT-2 (0.0065 min^{-1}), FIT-3 (0.0046 min^{-1}) are in the ratio 1.00:0.67:0.51.

for route, and Fig. 6(b) for route 2. One major peak between 340 and 520 nm, λ_{max} = 395 nm, was observed for all resulting solutions collected from 0 to 50 min. The intensity of PL was normalized before the calculation of photocatalytic degradation rate constant (k_{cat}). Theoretically, the slope value (R) obtained from the plot of $\ln(c/c_0)$ vs. time (min) will be equal to the photocatalytic degradation rate constant (k_{cat}). The k_{cat} values for the two degradation routes are given as follows. In route 1, the k_{cat} values for FIT-1 (0.252 min^{-1}), FIT-2 (0.154 min^{-1}), FIT-3 (0.113 min^{-1}) are in the ratio of 1.00:0.61:0.45, (Fig. 6(c)). In route 2, the k_{cat} values of FIT-1 (0.0196 min^{-1}), FIT-2 (0.0129 min^{-1}), FIT-3 (0.0101 min^{-1}) are in the ratio of 1.00:0.67:0.51, (Fig. 6(d)). The k_{cat} value of route 1 is ~30 times higher than that of route 2. The ratio of k_{cat} is very similar in the two routes. The Michaelis–Menten kinetic equation show that the turn-over number, TON, equals to k_{cat} (min^{-1}) in a high concentration of substrate [23,24]. The TON of route 1 is in the range of 0.225 and 0.113, which satisfy the requirement of industrial standard, $10^{-1} < TON < 10^2$ [20]. Furthermore, in the FIT-1 experiments, the highest catalytic efficiency and maximum photo-degradation rate were recorded. It is clear that increase of the iron oxide amount in FIT cannot improve the photocatalytic activity of AA over FIT.

(III) Spectrum study for photcatalytic products

In theory, the final mineralized product of organic acid species is regarded as CO_2 and H_2O. The final mineralization product CO_2 is detectable, if the initial concentration of adsorbed organic acid species can reach 1×10^{-4} M or higher [15]. Unfortunately, in this case, the adsorbed concentration of AA is less than 6.6×10^{-6} M. Therefore, we employed ^{13}C NMR, FT-IR, and LC–mass spectra to clarify the structures of compounds after the 60 min UV irradiation, instead of measuring the final products, CO_2 and H_2O.

(a) The ^{13}C NMR spectra and FT-IR spectra

The samples for ^{13}C NMR spectra measurement were prepared in DMSO. In comparison with the stock sample, two phenomena were observed. First, the peak intensity of carboxylic acid, located at ~170 ppm, decreases about ~10% (FIT-3), ~12% (FIT-2), and ~70% (FIT-1), respectively, for the samples irradiated by UV lights. Second, a new peak located at ~205 ppm, assigned for —CHO group of benzaldehyde, is recorded in the FIT-2 and FIT-3. The ^{13}C NMR spectra show that the de-carboxylation reaction mainly occurred in FIT-1 route, and the carbonyl reduction reaction is initialized in the FIT-2, and FIT-3 routes.

Beside ^{13}C NMR measurement, the samples were characterized by FT-IR simultaneously. Fig. 7(a) shows the FT-IR spectrum of the product isolated from FIT-1 route. Twelve peaks match the characteristic modes of aniline. On the other hand, the FT-IR spectrum for the product isolated from FIT-2/FIT-3 route, (Fig. 7(b)), shows seven recorded characteristic modes of 2-aminobenzaldehyde, (Fig. 7(b)).

(b) LC–mass spectra

In the LC–mass spectra for the photo-catalytic products collected at the 60th min, the m/e data reveal that polymerization of products is generally occurred in all samples. However, the photo-degradation mechanisms still can be derived from the collected m/e data. In the route of FIT-1, the m/e data suggest that the de-carboxylation reaction prevails. Nevertheless, the alkaline environment favors the hydroxylation addition when the de-carboxylation reaction has conducted. The resulting products are aniline, and 4-aminophenol. In the routes of FIT-2, and FIT-3, the recorded product is 2-aminobenzaldehyde. The carbonyl reduction is believed to be the main reaction in these routes. Since benzene is collected in all catalytic routes, the de-amination reaction should be initialized in all

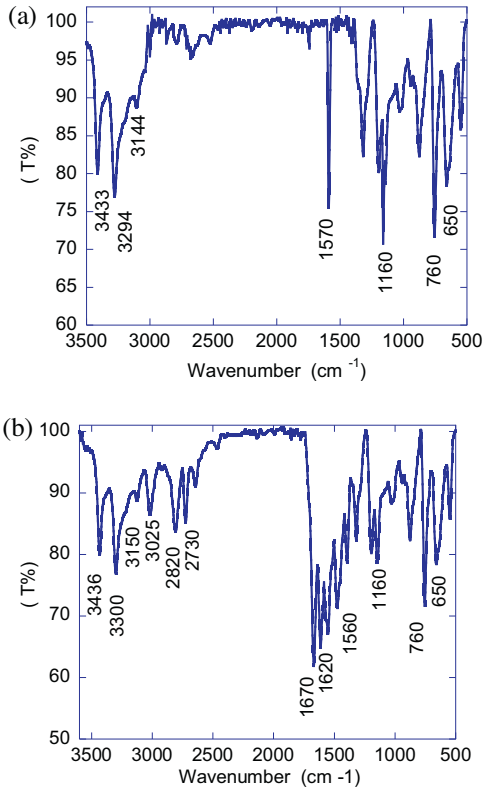

Fig. 7. FT-IR spectra for product isolated from (a) AA over FIT-1 (b) AA over FIT-2/FIT-3. In (a), 7 characteristic modes of aniline are recorded. In (b), 12 peaks match the characteristic modes of 2-aminobenzaldehyde.

FIT involved reactions. The proposed polymerization mechanisms based on the m/e data observed in LC–mass spectra are given in the following paragraph.

(IV) The proposed photo-degradation mechanisms

(a) In FIT-1 spectrum

In the route of FIT-1, four peaks, m/e = 136, 173, 283, and 295, shown in Fig. 9(a), are recorded in the LC/mass spectrum. The m/e = 136 peak is attributed to un-reacted AA. The peaks for m/e = 173, 283, and 295 are contributed by the polymerization of photo-degraded products, as shown in Eqs. (a-1), and (a-2). The m/e values recorded in Fig. 8(a) suggest that the polymerization between benzene, aniline, and 4-aminophenol are the main reactions in this route. Therefore, mechanisms for products are classified into two portions, i.e. photo-degradation and polymerization.

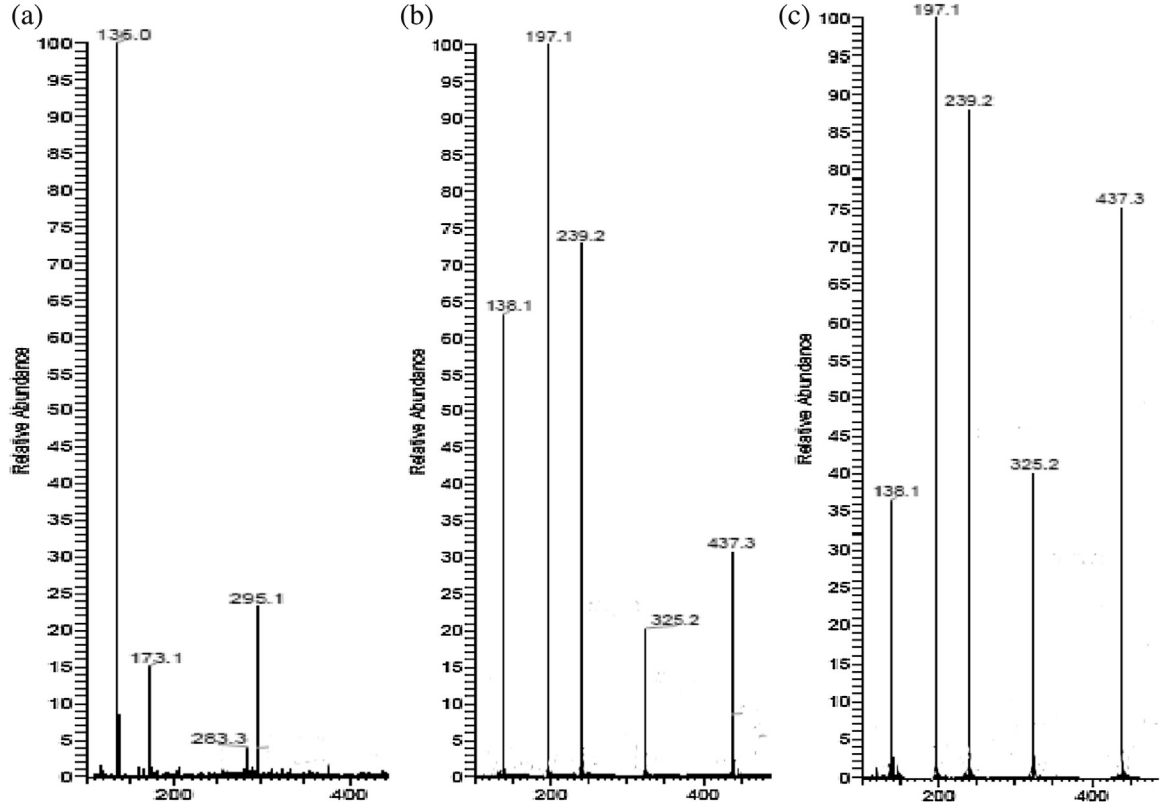

Fig. 8. LC–mass spectra. (a) FIT-1 spectrum: four peaks, m/e = 136, 173, 283, and 295, are shown. (b) FIT-2 spectrum, and (c) FIT-3 spectrum, five peaks, m/e = 138, 197, 239, 325, and 437, are observed.

Products from photo-degradation

(a-1) AA → 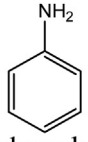 → 

(de-carboxylation) (de-amination)

(a-2) AA → 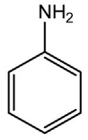 → 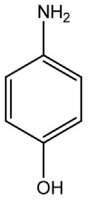

(hydroxylation addition)

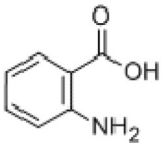 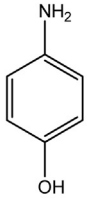 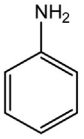

AA= anthranilic acid 4-aminophenol aniline

Products from polymerization

(a-3)  + 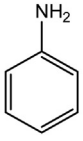 → 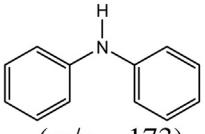 + H_2

(m/e = 173)

(a-4) 3 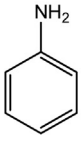 → 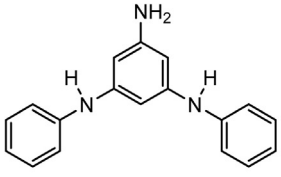 + 2 H_2

(m/e = 283)

(a-5) 2 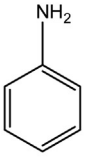 + 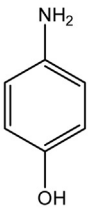 → 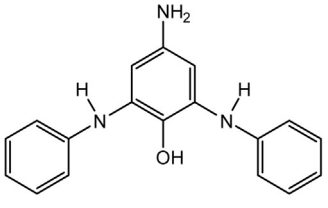 + 2H_2

(m/e = 295)

(b) In FIT-2 and FIT-3 spectra

Five peaks, m/e = 138, 197, 239, 325, and 437, are recorded in LC–mass spectrum for FIT-2, Fig. 8(b), and FIT-3, Fig. 8(c), respectively. The peak of m/e = 138 stands for the un-reacted AA. The m/e = 197, 239, 325 and 437 are contributed by the polymerization of photo-degraded products. In this route, the carbonyl reduction of AA is preferential. The observed product is 2-aminobenzaldehyde. Nevertheless, the de-carboxylation reaction and the de-amination are also occurred in this route. The observed product is benzene. The polymerization between benzene and 2-aminobenzaldehyde is the major reaction in FIT-2 and FIT-3 routes.

Products from photo-degradation

(b-1) AA → 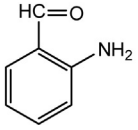 (carbonyl reduction) (Major)

2-aminobenzaldehyde

(b-2) AA → 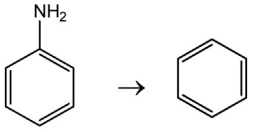 (de-amination) (Minor)

Benzene

Products from polymerization

(b-3) 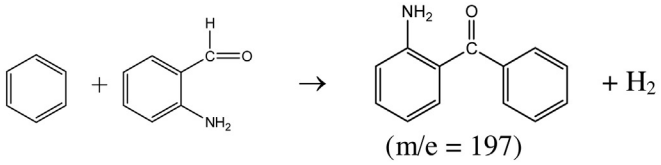

(m/e = 197)

(b-4) 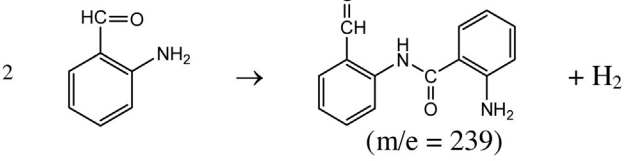

(m/e = 239)

(b-5) 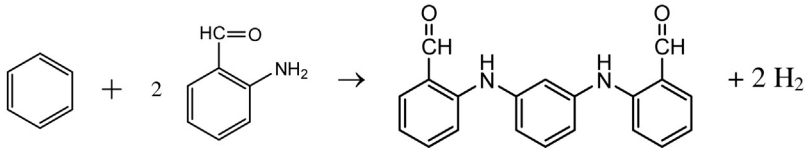

(m/e = 325)

(b-6) 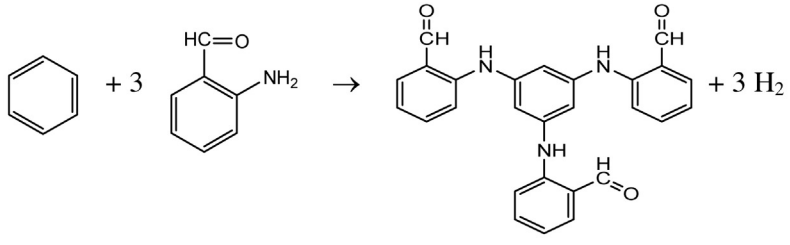

(m/e = 437)

4. Discussion

4.1. The effect of TPAB in the oxidation state of iron

In previous study, we reported that TPAB [$N(n\text{-}Pr)_4^+Br^-$] is able to dissociate the vanadyl bond of V_2O_5 monomer on the surface of TiO_2 nanoparticle [15]. In this study, the XPS data show that TPAB still plays a reducing reagent in the reduction of Fe_2O_3 monomers. The suggested mechanism is given in Scheme 1. The detail explanation is in the following paragraphs.

(I) At the beginning of reduction, ($N(n\text{-}Pr)_4^+$) initializes an electronphilic attack to the terminal oxygen of Fe_2O_3, [O═(Fe^{3+}—O—Fe^{3+})═O], to form a 6-member ring structure

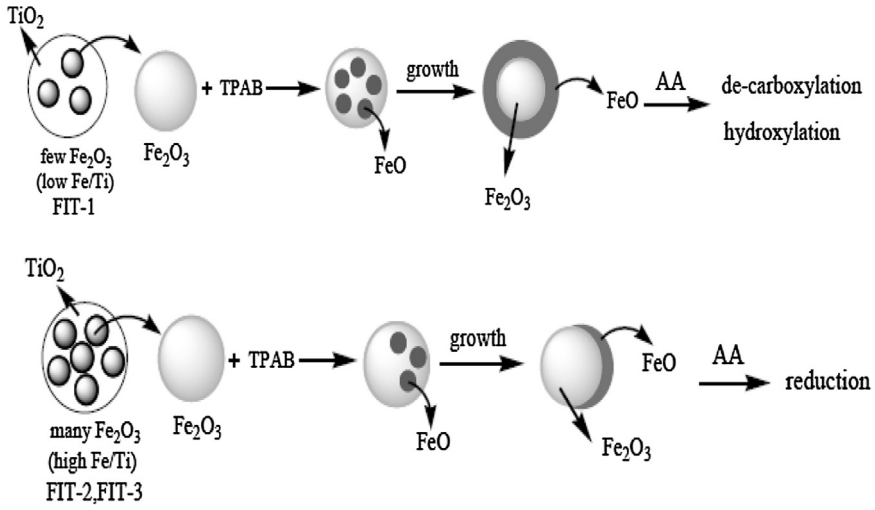

Fig. 9. The illustrated mechanism for the growth of FeO in Fe_3O_4 (FeO/Fe_2O_3) matrix of (a) FIT-1, (b)FIT-2, and FIT-3.

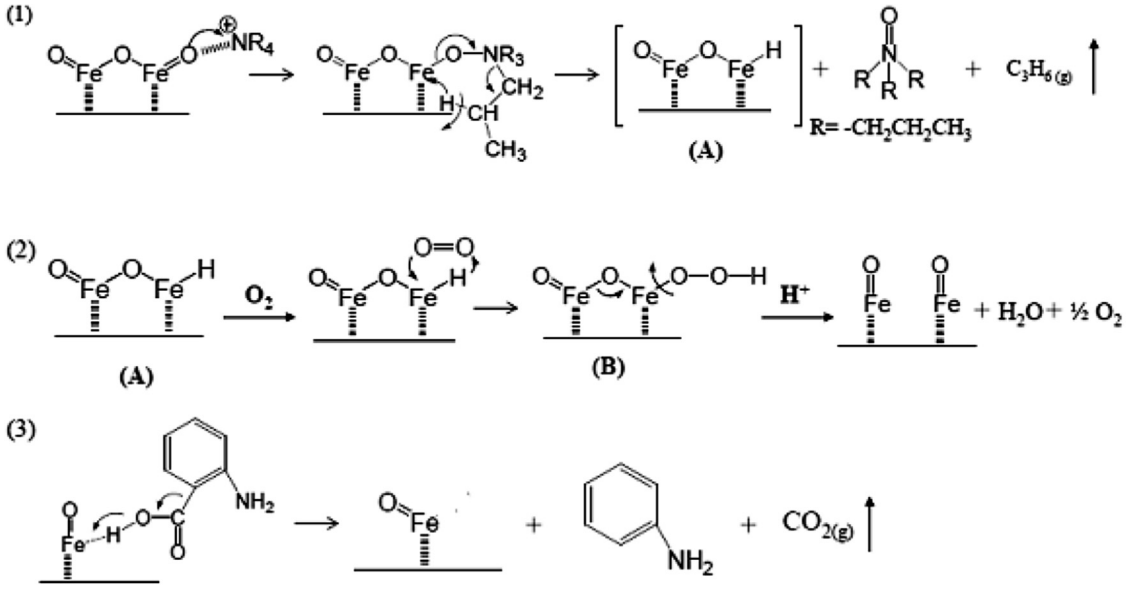

Scheme 1. Mechanism of dissociation of iron oxide on FIT nanoparticles.

on TiO_2-(0 0 1). The hydrogen of β carbon of propyl group in $N(n\text{-}Pr)_4^+$ start a nucleophilic attack to the iron atom of terminal Fe=O group. The terminal iron atom adopts the hydrogen in β-carbon of propyl group, and the terminal oxygen of [O=(Fe^{3+}–O–Fe^{3+})=O] is removed by $N(n\text{-}Pr)_3$, to form a good leaving group O=$N(n\text{-}Pr)_3$, simultaneously [15]. The resulting product is [H–(Fe^{2+}–O–Fe^{3+})=O], denoted as compound (A), and the co-product is C_3H_6(g), shown in Scheme 1, step 1. The co-product C_3H_6(g) is unable collected, but the O=N(n-Pr) product can be detected from the solvent. The IR spectrum for the collected solvent shows the characteristic O=N stretching at 1592 cm^{-1}, which confirms the existence of O=N(n-Pr) in the solvent [15,21].

(II) The compound (A), [H–(Fe^{2+}–O–Fe^{3+})=O], is easily oxidized by O_2 molecule from atmosphere. The O_2 molecule attacks the terminal H of compound (A) to form a 4-member ring. In the acidic situation, the terminal hydrogen is rapidly removed to form [(•Fe^{2+}–O–Fe^{3+})=O] radical, denoted as compound (B), shown in Scheme 1, step 2. The compound (B) is dissociated to two FeO monomers by kinetic equilibrium, because the concentration of compound (B) grows. The FeO monomers incorporate with neighboring Fe_2O_3 to form a stable Fe_3O_4 matrix. The reaction keeps going until the equilibrium lost [22,23].

Since TPAB is a limiting reagent, the amount of FeO monomer created by TPAB is restricted. Therefore, in the low ratio of Fe/Ti sample, the Fe_2O_3 monomers could be mostly convert to FeO. Therefore, the ratio of Fe^{2+}/Fe^{3+} is high. On the contrary, in the high atomic ratio of Fe/Ti sample, the Fe_2O_3 monomers are only partially converted to FeO. The atomic ratio of Fe^{2+}/Fe^{3+} is low. The XPS deconvolution data confirms this fact. The atomic ratio of Fe^{2+}/Fe^{3+} in FIT-1 is up to 1.99. The surface of Fe_3O_4 matrix in FIT-1 is reduced to FeO completely. On the other hand, in FIT-2 (1.35) and FIT-3 (1.17), the surface of Fe_3O_4 matrix is partially reduced to FeO. The evolution of iron oxide domain is illustrated in Fig. 9.

4.2. The mechanism of photo-selectivity of AA over FIT

(I) The capture of photogenerated electron (e^-) and hole (h^+)

Metal oxide doped TiO_2 is a photo-sensitive catalyst. When an electron–hole (e–h) pair is created by 365 nm UV (3.39 eV) irradiation, the photogenerated (e^-) from the top level of TiO_2 valence band (VB, +3.0 eV) is activated to reach the bottom level of TiO_2 conduction band (CB, −0.2 eV), band gap ~3.2 eV [14,24]. When the relaxation of excited electrons starts, the excited electrons are released from TiO_2 CB, (-0.2 eV) and are temporarily trapped

in Fe_3O_4 matrix, either in e_g of FeO (+0.3 eV), (FIT-1) or t_{2g} of Fe_2O_3 (+2.5 eV) (FIT-2, FIT-3), before reach the TiO_2 VB (+3.0 eV) [14,15,25]. The photogenerated (e^-) and (h^+) pair is thus delayed.

$$_{(s)}(\text{FIT-1})_{(s)} \rightarrow (e^-)_{(s)}\,(\text{FIT-1})_{(s)}\,(h^+)$$

(II) The de-carboxylation reaction

The hydroxyl radicals (•OH) and hydroxyl ions (OH—) play an influential role in the initialization of decarboxylation of AA. In FIT-1 route, the low spin (LS) state FeO site of FeO/Fe_2O_3 is able to adopt the photo-generated (e^-) by empty e_g orbital. The stable LS Fe^{2+} is temporarily reduced to unstable Fe^+. At this moment, Fe^+ acts as an electron-rich Lewis base, and is able to donate the adopted electron quickly, Scheme 1, step 3. The reduction of the oxygen molecules adsorbed on the surface of FIT-1 with the available trapped electrons (e^-) starts: $O_2 + e^- \rightarrow O_2^{\bullet -}$. The $O_2^{\bullet -}$ ions then react with proton ion of —COOH group of adsorbed AA molecules to create HO^- ions and (•OH) radicals: $2\,O_2^{\bullet -} + 2\,H^+ + e^- \rightarrow OH^- + {}^{\bullet}OH + O_2$. The unstable (•OH) radicals are quickly reduced to OH^- groups. At this step, the abundant OH^- ions are able to consume all available proton ions of —COOH group of AA. Therefore, a following chain-reaction of bond cleavage makes the —COO group as a leaving group. The photo-initialized de-carbonation reaction of AA over FIT-1 keeps going until OH^- ions is no longer available: $HOOC—(C_6H_4)—NH_2 + OH^- \rightarrow H—(C_6H_4)—NH_2 + OH^- + CO_2$ [15,26].

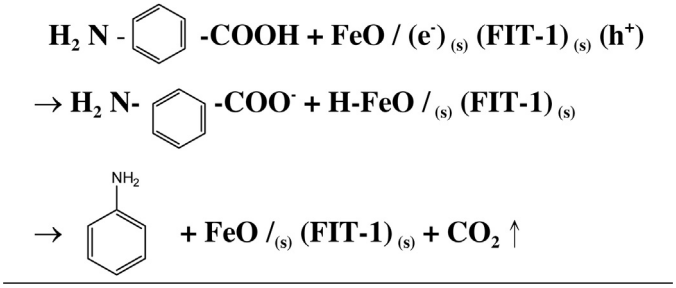

(III) The hydroxylation addition

The hydroxylation addition is the other possible reaction in an alkaline environment. The para-addition of —OH group to aniline, i.e. hydroxylation reaction, has the priority to be performed, when the nitrogen atom of aniline adsorbed on the surface of FIT-1 with the Lewis base (FeO/Fe_2O_3) moiety, as shown in the following equation.

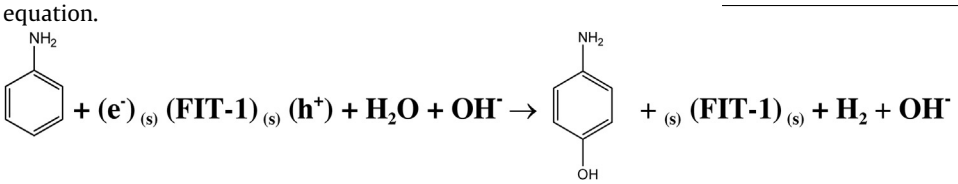

(IV) The carbonyl reduction reaction

In FIT-2, and FIT-3 routes, the FeO moiety of FeO/Fe_2O_3 still proceeds the de-protonation reaction. If the LS Fe^{3+} ion of Fe_2O_3 adopts the photo-generated (e^-) by t_{2g} orbital, the LS Fe^{3+} is reduced to stable LS Fe^{2+}. The lone pair electrons of (:FeO) attract the proton ion of H_2O to form (H:FeO) and OH^- ion. The H atom of (H:FeO) attack the C atom of —COOH group to form the C—H bond. At this moment, LS Fe^{2+} acts as a Lewis acid to attack the other oxygen atom of —COOH group. This electrophilic attack leads to the bond cleavage between the anion oxygen and C atom. Then, the OH^- leaves and —(H)C=O is formed. The mechanism is given in the follows.

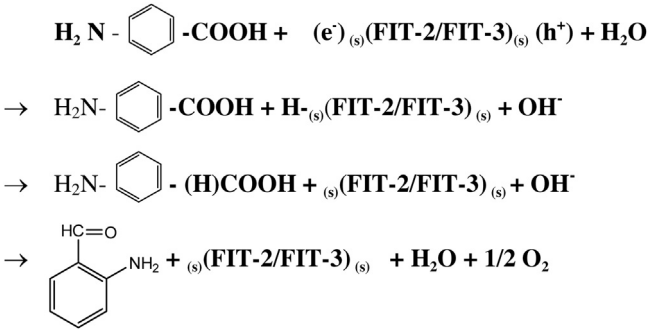

(V) The de-amination reaction

The de-amination reaction is induced by the reduction of the nitrogen atom of aniline adsorbed on the surface of FIT. The oxygen atom of water molecule performs a nucleorphilic attack to C atom bonded to N atom of NH_2 group. The following reaction is H atom of H_2O to attack the N atom of NH_2 group. The NH_2 group is reduced to NH_3 as a good leaving group. The H_2O lost one H atom and substitutes the position of NH_2 at the benzene ring. After the SN_2 substitution, the temperate product is phenol. The FeO domain of FIT performs an electrophilic attack to oxygen atom of OH group. The OH group is replaced by H atom, and the FeO is oxidized to Fe_2O_3. The de-hydroxylation reaction has finished. The final product is benzene.

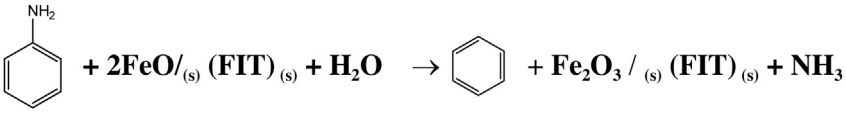

5. Summary

In this paper, we report a newly developed FIT photocatalyst with tunable photocatalytic selectivity in photo-degradation of AA. The photo-degradation selectivity is controlled by the atomic ratio of Fe^{2+}/Fe^{3+} in FIT. In low atomic ratio of Fe/Ti route (i.e. high Fe^{2+}/Fe^{3+} ratio), the de-carboxylation reaction is the dominate selectivity to perform the photo-degradation. On the other hand, a high Fe/Ti ratio with low Fe^{2+}/Fe^{3+} ratio is necessary for the initialization of carbonyl reduction. The photo-induced ($e^- – h^+$) pair and (FeO/Fe_2O_3) moiety in FIT can substitute the roles of [HO^-] and [•OH] in the photo catalytic reaction. The yield of too many hydroxyl radicals in the photo Fenton reaction is able to be avoided in the treatment of environmental organic pollutants or biological application.

Acknowledgments

The research is partially supported by Ministry of Science and Technology, Taiwan, ROC under the contract number NSC 102-2622-M-415-001-CC3 and MOST-103-2622- M-415-001-CC3. Authors thank Mr. Ren-Xing Rai for the help in Chem Draw.

References

[1] R. Bauer, G. Waldner, H. Fallmann, S. Hager, M. Klare, T. Krutzler, S. Malato, P. Maletzky, Catal. Today 53 (1999) 131–144.
[2] J. Herney-Ramireza, M.A. Vicenteb, L.M. Madeirac, Appl. Catal. B 98 (2010) 10–26.
[3] M. Pera-Titus, V. Garcí-Molina, M.A. Baños, J. Giménez, S. Esplugas, Appl. Catal. B 47 (2004) 219–256.
[4] M. Pelaeza, N.T. Nolanb, S.C. Pillai, M.K. Seeryc, P. Falarasd, A.G. Kontosd, P.S.M. Dunlope, J.A. Hamiltone, K. O'sheaf, M.H. Entezarig, D.D. Dionysioua, Appl. Catal. B 125 (2012) 331–349.
[5] H.J.H. Fenton, J. Chem. Soc. Trans. 65 (1894) 899–911.
[6] S. Goldstein, D. Meyerstein, G. Czapski, Free Rad. Biol. Med. 53 (1993) 435–445.
[7] Y. Luo, E.S. Henle, S. Linn, J. Biol. Chem. 271 (1996) 21167–21176.
[8] J.A. Imlay, S.M. Chin, S. Linn, Science 240 (1988) 640–642.
[9] W. Wu, X. Xiao, S. Zhang, F. Ren, C. Jiang, Nanoscale Res. Lett. 6 (2011) 533–547.
[10] Y. Li, J.S. Wu, D.W. Qi, X.Q. Xu, C.H. Deng, P.Y. Yang, X.M. Zhang, Chem. Commun. 5 (2008) 564–566.
[11] W.S. Tung, W.A. Daoud, ACS Appl. Mater. Interfaces 1 (2009) 2453–2461.
[12] C.-S. Yang, C.-J. Chen, Appl. Catal. A 294 (2005) 40–48.
[13] C.-S. Yang, Y.-J. Wang, M.-S. Shih, Y.-T. Chang, C.-C. Hon, Appl. Catal. A 364 (2009) 182–190.
[14] C.-C. Ou, C.-S. Yang, S.-H. Lin, Catal. Sci. Technol. 1 (2011) 295–307.
[15] S.-H. Lin, C.-C. Ou, M.D. Su, C.-S. Yang, Catal. Sci. Technol. 3 (2013) 2081–2091.
[16] (a) JCPDS, 21–1272.;
(b) JCPDS, 29–1360.
[17] D. Gazzoli, G. Mattei, M. Valigi, J. Raman Spectrosc. 38 (2007) 824–831.
[18] C. Baratto, P. Lottici, D. Bersani, G. Antonioli, J. Sol–Gel Sci. Technol. 13 (1998) 667–671.
[19] J.F. Moulder, W.F. Stickle, P.E. Sobol, K.D. Bomben, Handbook of X-ray Photoelectron Spectroscopy, PerkinElmer Corporation, Norwalk, CT, 1992.
[20] L. Michaelis, M.L. Menten, Z. Biochem, (1913) 333–369.
[21] G. Socrates, Infrared Characteristic Group Frequencies, Wiley, New York and London, 1980.
[22] M.J. Tiernan, P.A. Barnes, G.M.B. Parkes, J. Phys. Chem. B. 105 (2001) 220–228.
[23] E.R. Monazam, R.W. Breault, R. Siriwardane, Energy Fuels 28 (2014) 5406–5414.
[24] A.G. Thomas, W.R. Flavell, A.K. Mallick, A.R. Kumarasinghe, D. Tsoutsou, N. Khan, C. Chatwin, S. Rayner, G.C. Smith, Phys. Rev. B 75 (2007) 035105.
[25] J. Tang, M. Myers, K.A. Bosnick, L.E. Brus, J. Phys. Chem. B 107 (2003) 7501–7506.
[26] A.R. Khataee, M.B. Kasiri, J. Mol. Catal. A: Chem. 328 (2010) 8–26.